Endogenous Optical Biomarkers of Ovarian Cancer Evaluated with Multiphoton Microscopy

Nathaniel D. Kirkpatrick,[1] Molly A. Brewer,[2] and Urs Utzinger[1]

[1]Biomedical Engineering Program, University of Arizona, Tucson, Arizona; and [2]University of Connecticut Health Center, Farmington, Connecticut

Abstract

Purpose: **Among gynecologic cancers, ovarian cancer is the second most common and has the highest mortality. Currently, there is no accurate early diagnostic technique for ovarian cancer. Furthermore, little is understood regarding the early progression of this disease. We have imaged multiphoton interactions of endogenous tissue constituents from normal and abnormal ovarian biopsies that were kept viable during transport from the operating room and microscopy.**

Experimental Design: **The ovarian surface and underlying stroma were assessed with two-photon excited fluorescence (2PEF) and second harmonic generation (SHG). High-resolution, optically sectioned images were analyzed for epithelial morphology based on 2PEF and collagen density and structural integrity based on SHG. Additionally, multiwavelength 2PEF provided an estimation of the cellular redox ratio of epithelial cells.**

Results: **Normal tissue exhibited a uniform epithelial layer with highly structured collagen in the stroma, whereas abnormal tissue exhibited varied epithelium with large cells and substantial quantitative changes to the collagen structure. Samples from patients at high risk for developing ovarian cancer (based on their personal/family history of cancer) exhibited highly variable cellular redox ratios and changes in collagen structure that trended toward cancer samples.**

Conclusion: **This study highlights differences in endogenous signals in viable ovarian biopsies based on quantitative collagen structural changes and redox ratio estimates that may lead to improved detection and further insights in ovarian cancer, particularly in the early stages of the disease.** (Cancer Epidemiol Biomarkers Prev 2007;16(10):2048–57)

Introduction

Epithelial ovarian cancer is the second most common gynecologic cancer with the highest mortality among gynecologic cancers (1). A disease with nonspecific symptoms, epithelial ovarian cancer typically is diagnosed in late stages when cure is 30% or less rather than at an early stage when cure is 80% or better (2). Furthermore, little is understood in the progression of epithelial ovarian cancer from early to late stage (3, 4). It is therefore imperative to better understand the fundamental changes in ovarian carcinogenesis to develop early diagnostic measures for ovarian cancer that could improve the outcome of the disease.

Serum markers for diagnosing ovarian cancer have been the focus of research for several decades, starting with the CA-125 (5), with additional combinations of markers evaluated recently (6, 7). However, these markers result in relatively poor sensitivity and specificity, and it is not clear how early they can detect the disease (4). One approach has been to use multiple markers in combination (7, 8), but effective combinations may vary for every patient. Imaging modalities such as computed tomography, magnetic resonance imaging, and ultrasound are effective at detecting ovarian cancer in later stages (9, 10), but have not achieved the sensitivity necessary for the detection of early ovarian cancer or precancer (8).

In other epithelial derived cancers, optical techniques including fluorescence spectroscopy of endogenous intracellular and extracellular constituents have shown potential for clinical cancer detection (11-13). Therefore, interrogating the endogenous optical signals of the ovarian surface has the potential to improve detection of the ovarian cancer (14). It is essential to define the key endogenous contrast constituents within the surface of the ovary and describe how these constituents correlate with changes related to carcinogenesis. Moreover, for a thorough understanding of the endogenous contrast present in early stages of the disease, high three-dimensional resolution is required to examine the optical epithelial and stromal signatures in normal and cancerous ovaries as well as ovaries from patients at high risk for developing ovarian cancer.

Recently, multiphoton microscopy has been shown to be a powerful tool to image endogenous contrast in tissue (15, 16) and has been used for *in vivo* cancer imaging (17, 18). Multiphoton microscopy has several advantages over traditional confocal microscopy, providing high-resolution images at increased imaging depths, minimal out-of-plane absorption, and inherent optical sectioning. With a tunable near-IR laser source, multiphoton microscopy also provides simultaneous endogenous contrast through cellular two-photon excited

Received 1/11/07; revised 7/2/07; accepted 8/7/07.

Grant support: NIH CA098341.

The costs of publication of this article were defrayed in part by the payment of page charges. This article must therefore be hereby marked *advertisement* in accordance with 18 U.S.C. Section 1734 solely to indicate this fact.

Requests for reprints: Nathaniel D. Kirkpatrick, 1656 E. Mabel St. Tucson, AZ 85724. Phone: 520-626-8767. E-mail: nkirk@email.arizona.edu

doi:10.1158/1055-9965.EPI-07-0009

fluorescence (2PEF) and extracellular second harmonic generation (SHG) contrast of collagen fibrils (15, 19) as well as exogenous contrast with 2PEF of contrast agents such as green fluorescent protein (20) or SHG of styryl dyes (21).

When imaging endogenous contrast using 2PEF and SHG, several fluorophores and scatterers are the source of the majority of the signal. In 2PEF, intracellular fluorescence arises primarily from NAD(P)H (NADH and NADPH) and FAD and can provide an estimate of a metabolism-related redox ratio (22-24). Extracellular 2PEF signal arises primarily from collagen and elastin; however, the main source of multiphoton contrast in the extracellular matrix is SHG resulting from the highly repetitive structure of type I fibrillar collagen (16, 25).

In this study, we applied multiphoton imaging to viable ovarian biopsies. Although it is possible to measure tissues during a short period following the removal of the blood supply with few resulting changes in fluorescence signals (26), we have developed a tissue incubation/imaging system that improves flexibility for measuring tissue obtained in the operating room and offers consistency in signals linked to cellular metabolism. Based on morphologic analysis of images from the ovarian surface as well as structural changes observed in collagen and redox estimates from epithelial cells, we present results comparing optical signatures between normal ovaries and ovaries from patients diagnosed with ovarian cancer. We also compared ovaries from patients at a low risk with those from patients at high risk for developing ovarian cancer, and we observed differences in cellular redox ratios and collagen structure between these groups.

Materials and Methods

All human investigations reported here were approved by the Institutional Review Board of the University of Arizona in accordance with an assurance filed with and approved by the Department of Health and Human Services. Before measurements, informed consent was obtained from each subject.

Tissue Incubating/Imaging System. A transportable system was developed for biopsy incubation and subsequent microscopic imaging. This system consisted of an incubation/imaging chamber maintained at 37°C and perfused with oxygenated, optically inert media (Fig. 1). We formulated an optically inert media with a similar solute concentration as commercial culture media and metabolic substrates for the tissue (1× PBS, 46 mmol/L glucose, 4 mmol/L L-glutamine) not only to minimize background signal and light reabsorption due to the media but also to preserve signals that would be seen with well-perfused tissue. Following surgical removal of the ovary laparoscopically or with laparotomy, biopsies were placed onto a coverslip with tissue adhesive and immediately submerged in the incubation chamber at 37°C. The portable incubation system was designed such that during transport to the microscope and imaging, the system remained at physiologic temperature with continuous flow of oxygenated culture media.

Multiphoton Imaging Setup. Samples were imaged with a Zeiss LSM 510 NLO upright laser-scanning microscope (Carl Zeiss) coupled to a Mira 900 150-fs pulsed titanium-sapphire laser (Coherent). Incident light was focused, and emitted signals were collected with a 20×/0.95 numerical aperture long working distance physiology objective (XLUMPFL20XW, Olympus). The laser was centered at λ_{inc} = 780 nm to excite NADPH- and FAD-related 2PEF as well as efficiently generate collagen SHG. 2PEF and SHG signals were collected in epifluorescence configuration, split with dichroic mirrors, through custom multiphoton bandpass filters ($2PEF_{blue}$ = 400-500 nm; $2PEF_{green}$ = 500-600 nm; SHG = 380-400 nm; Chroma) and guided onto non-descan PMT detectors (based on R6357, Hamamatsu). Our 2PEF filters were chosen to maximize discrimination between NADPH and FAD fluorescence (23). Image stacks were collected from the ovarian surface up to 200 μm into the underlying stroma.

Rapid Tissue Viability Assessment. To determine the viability of the tissue following imaging, we developed a rapid method based on two water-soluble dyes: propidium iodide (PI) and acridine orange (AO;

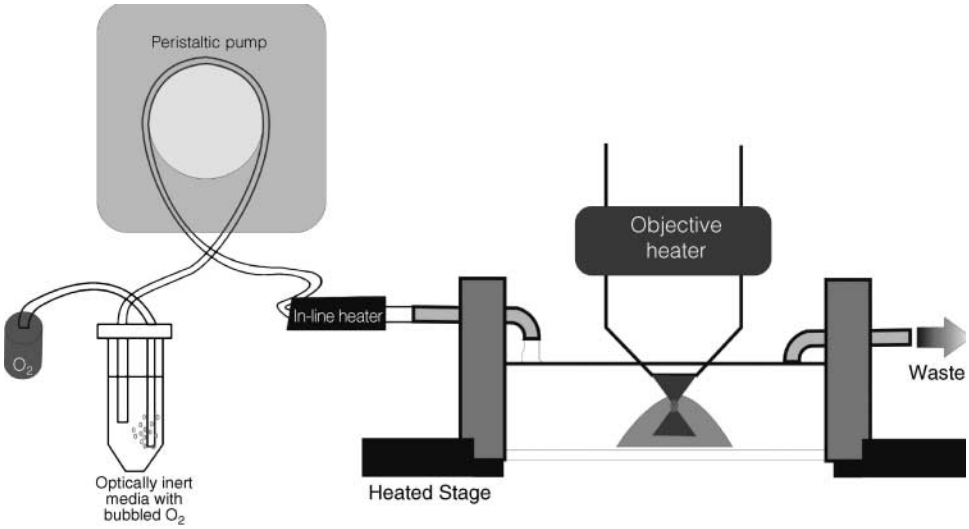

Figure 1. Schematic of *in vitro* incubation/imaging system. Biopsies were placed in an open chamber and perfused with heated and oxygenated optically inert media. The chamber was adapted for attachment to the microscope, and the stage was heated in addition to the media for a stable temperature. Multiphoton images were collected with a physiology lens dipped into the media.

Molecular Probes). PI (λ_{em} = 630 nm) preferentially stains the nucleus of cells with compromised plasma membranes. AO (λ_{em} = 520 nm when bound to DNA) indiscriminately enters cells through passive diffusion and binds nucleic acids. The concentration of PI was optimized to maximize PI binding in membrane-compromised cells compared with AO. Following 2PEF and SHG imaging, samples were incubated in a solution of AO (100 nmol/L) and PI (3.3 μmol/L) for 5 min and then reimaged at 488 nm argon laser excitation to provide immediate feedback on viability.

Viability Verification. Murine ovary biopsies were removed after sacrifice of the animals and directly placed into the incubation system. Biopsies were stained every 30 min with the AO/PI-based live/dead cell stain. Image stacks were subsequently collected from the ovarian surface down to 100 μm into the stroma. The number of red (compromised, PI stained) cells and green (viable, AO stained) cells for each optical slice were then quantified.

Confirmation of NADPH-Related 2PEF. Intracellular NAD(P)H-related 2PEF was confirmed by introducing sodium cyanide (NaCN, 8 mmol/L) into the media. NaCN blocks the electron transport chain in the mitochondria, resulting in a buildup of NAD(P)H and a corresponding increase in fluorescence intensity associated with NAD(P)H (22). Cellular fluorescence before and after NaCN treatment was calculated in the cellular regions from each image.

Intracellular Emission Standards. NADH (Sigma-Aldrich), a standard for both NADPH and NADH because of their spectral similarities (27), was dissolved in 1× PBS to a final concentration of 10 mmol/L and 2PEF (λ_{ex} = 780 nm) of NADH was collected with a 40× 1.3 numerical aperture oil immersion objective (Carl Zeiss). The $2PEF_{blue}$ channel and $2PEF_{green}$ channel were measured with equal gain on each PMT. The gain was set by optimizing the signal intensity in the $2PEF_{blue}$ channel because the emission maximum of NADH lies within the range of this channel. FAD (Sigma-Aldrich) was dissolved in 1× PBS for a final concentration of 10 mmol/L and imaged similarly to NADH with optimization of signal intensity in the $2PEF_{green}$ channel because the emission maximum of FAD is located in this range.

Image Processing and Analysis. Images were processed with Matlab (Mathworks) except for three-dimensional image projections created with the Zeiss LSM Image Browser. For visual presentation, images were optimized by background thresholding and histogram stretching. In some cases, we observed hyperintense punctate 2PEF, often masking diffuse intracellular 2PEF, associated primarily with the ovarian epithelial surface. Punctate 2PEF has been previously reported in tissue, but its origins are unknown (28) and most likely serve minimal diagnostic value. To enhance epithelial cell morphology, 2PEF images were acquired with intensity saturation in the location of the punctate structures and high signal (but unsaturated) in regions consistent with intracellular fluorescence. In the postprocessing of these images for visualization, the saturated pixels were selected and replaced with random values in the range of the image background intensity. Additionally, neighboring pixels (up to two pixels) of saturated pixels were included in the random value replacement to reduce sharp intensity transitions in the image. To overlay the pseudo-green 2PEF and grayscale SHG images into a single image for visualization, 2PEF pixels were combined with SHG pixels to form a colored image where the three individual color channels were defined as red = SHG, green = 2PEF + (1 − 2PEF) × SHG, and blue = SHG and then merged into an RGB image (i.e., SHG appeared grayscale, whereas 2PEF appeared green). Although these techniques improved visual image contrast and presentation, all quantitative image analysis was completed on the unprocessed images to avoid any artifacts introduced by the aesthetic image processing.

For collagen assessment based on SHG, we calculated the gray-level co-occurrence matrix (GLCM) of the SHG image. The GLCM provides texture features based on gray-level statistical patterns between neighboring pixels. In particular, the correlation feature, a measure of intensity correlation as a function of pixel distance, relates to collagen fibril structure by indicating fibril size and separation (29). The correlation was calculated for distances ranging from 1 to 30 pixels (2-60 μm) in the horizontal direction (vertical and diagonal correlations yielded similar results). For GLCM correlation calculations, regions in the SHG images were selected near the epithelial surface, and up to four consecutive optical slices (5-μm z steps) were averaged to create a correlation curve for each biopsy. Besides using the GLCM for texture analysis, we also assessed the spatial frequency content of the SHG images. Each image slice was projected into 180 angular projections (differing by 1°) with the radon transform. Next, the discrete Fourier transform was calculated for each projection resulting in the projection-slice Fourier transform. From the projection-slice Fourier transform, the spectral power of selected spatial frequency bands was calculated. Frequency bands of interest included low (excluding the DC component), middle, and high spatial frequencies.

Cellular redox estimates based on two-channel 2PEF of subcellular regions were calculated ratiometrically from estimated NAD(P)H- and FAD-related fluorescence to minimize interfering factors such as scattering and absorption (23). Assuming that intracellular fluorescence in the wavelength range 400 to 600 nm arises primarily from NAD(P)H and FAD, we predicted that 2PEF in the $2PEF_{blue}$ and $2PEF_{green}$ channels was proportional to the probed concentration of NAD(P)H and FAD contributions,

$$2PEF_{blue} \cong \alpha \times [NAD(P)H] + (1 - \alpha) \times [FAD]$$

$$2PEF_{green} \cong \beta \times [NAD(P)H] + (1 - \beta) \times [FAD]$$

where the $2PEF_{blue}$ channel is related to the concentration of NAD(P)H and FAD by a weighting factor α. Likewise, the $2PEF_{green}$ channel is related to the concentration of NAD(P)H and FAD by a weighting factor β. Using the NADH and FAD standard solution images (SNADH, SFAD), the contribution of each individual fluorophore to the two 2PEF channels ($2PEF_{blue}$ and $2PEF_{green}$) was computed from the average intensity ($2PEF_{blue,SNADH}$, $2PEF_{green,SNADH}$, $2PEF_{blue,SFAD}$, $2PEF_{green,SFAD}$). By

substituting the ratiometric values calculated for the NADH standard ($2PEF_{blue,SNADH}/2PEF_{green,SNADH}$, [FAD] = 0) with the ratios of the FAD standard ($2PEF_{blue,SFAD}/2PEF_{green,SFAD}$, [NADH] = 0), we solved for the α and β weighting factors. Finally, solving for NAD(P)H and FAD concentrations,

$$[\mathrm{NAD(P)H}] = \frac{(1-\beta)\times 2PEF_{blue} - (1-\alpha)\times 2PEF_{green}}{\alpha-\beta} \quad (A)$$

$$[\mathrm{FAD}] = \frac{\beta\times 2PEF_{blue} - 2PEF_{green}}{\beta-\alpha} \quad (B)$$

where the weighting factors were $\alpha = 0.72$ and $\beta = 0.15$.

Based on the calculated NAD(P)H and FAD contributions, the cellular redox was defined as a ratio between the two,

$$\mathrm{Redox} = \frac{\mathrm{FAD}}{\mathrm{FAD}+\mathrm{NAD(P)H}} \quad (C)$$

as previously described (22).

To be consistent in redox analysis of the surface epithelium, we developed a segmenting routine in Matlab to automatically separate the cellular regions from 1other 2PEF generating areas. For segmentation, the FAD concentration image (Eq. B) was calculated because of a strong contrast between FAD estimation in cellular regions and pseudo-FAD estimation in noncellular regions. By thresholding the FAD image at values consistent with cellular regions and converting the image to binary values, we generated a mask indicating the location of cells. This mask was cross-correlated with another binary image with circular dimensions approximately the size of a cell to smooth the mask image. After applying the mask, a user-defined manual cell selection removed any small noncellular regions adjacent to cellular regions. Finally, the pixel-by-pixel redox ratio as well as the average redox ratio (Eq. C, excluding any saturated pixels) was calculated for cellular regions in the image.

Statistics. All statistical analysis was done in the JMP software platform (SAS).

Histology. Following imaging, ovarian biopsies were fixed in 10% buffered neutral formalin for standard H&E staining. A careful diagram of the biopsies was made, and imaged regions were marked for histologic sectioning so that the section correlated with the imaged area. Sections selected from this diagram were read by a gynecologic pathologist to determine the diagnosis associated with the imaged region.

Results

To first test the incubation/imaging chamber, we examined the viability of tissue maintained in our system. For verification purposes, murine ovary biopsies (6 ovaries, 12 biopsies) were placed immediately in the incubation chamber after harvesting, and viability was assessed with our rapid AO/PI assay. We observed a substantial number of compromised cells after only 30 min in culture (Fig. 2A) but the proportion of compromised cells decreased with culture time compared with viable cells (Fig. 2B). From the ratio of compromised to viable cells, we found that the tissue underwent several stages following introduction into the incubation/imaging system (Fig. 2C). Initially, the tissue adjusted to the new *ex vivo* environment during a ''conditioning'' phase with a larger proportion of compromised cells staining with PI because of transient membrane permeability. However, as the tissue remained in the incubation chamber, the ratio of compromised to viable cells decreased exponentially, with a 30% reduction by 1 h and minimal compromised cells after 2 h. When ovaries at this sustained stage were exposed to 70% ethanol, the red/green viability ratio increased significantly consistent with cellular damage ($P = 0.003$, ANOVA linear contrast).

Next, ovarian biopsies from patients undergoing laparoscopic oophorectomy were measured with the system. On a subset of these biopsies, the viability was assessed following the imaging procedure. These biopsies consistently exhibited a majority of live cells with few compromised cells visible (Fig. 2D). Conversely, in ovaries difficult to excise during surgery resulting in a 45-min delay in introduction to the incubation system, we observed an increase in compromised cells (Fig. 2E). Based on the results of the initial murine AO/PI assays and experience with patient surgeries, all of the biopsies used for analysis were immediately placed in the incubation system following surgery and imaged during an optimal experimental window that started 45 min after sample removal and extended up to 4 h, allowing for flexible measurement times due to unpredictable surgery schedules and restricted microscope scheduling time.

We have imaged 53 ovarian biopsies from 31 patients in this study. Patients ranged in age from 28 to 73 years old and were pre-, peri-, or postmenopausal. Of the patients measured, 4 were diagnosed with ovarian cancer (5 biopsies), 1 with endometriosis (2 biopsies), and 25 with normal ovaries (46 biopsies). Additionally, normal patients were stratified by their risk status for developing ovarian cancer (normal-low or normal-high risk), a measure based primarily on the presence of germline mutations and family history of cancer. Due to handling error, several biopsies were excluded from analysis. Images lacking good signal to noise and samples missing key features such as the surface epithelium were excluded from analysis. For quantitative analysis of the collagen structure based on SHG, representative images from biopsies with the same magnification and image quality resulted in 26 samples from 25 patients. Those images included 5 cancer, 7 normal-low risk, 12 normal-high risk, and 2 samples of undetermined risk status (not used in risk status analysis). Redox estimates were calculated on a subset of 15 patients (37 samples) from multiple cellular regions per biopsy, resulting in 11 cancer, 7 normal-low risk, and 19 normal-high risk samples.

Intracellular 2PEF, extracellular 2PEF, and strong extracellular SHG were observed in the ovarian biopsies. An example of a normal ovarian surface is shown in Fig. 3A with highly organized epithelial cells forming

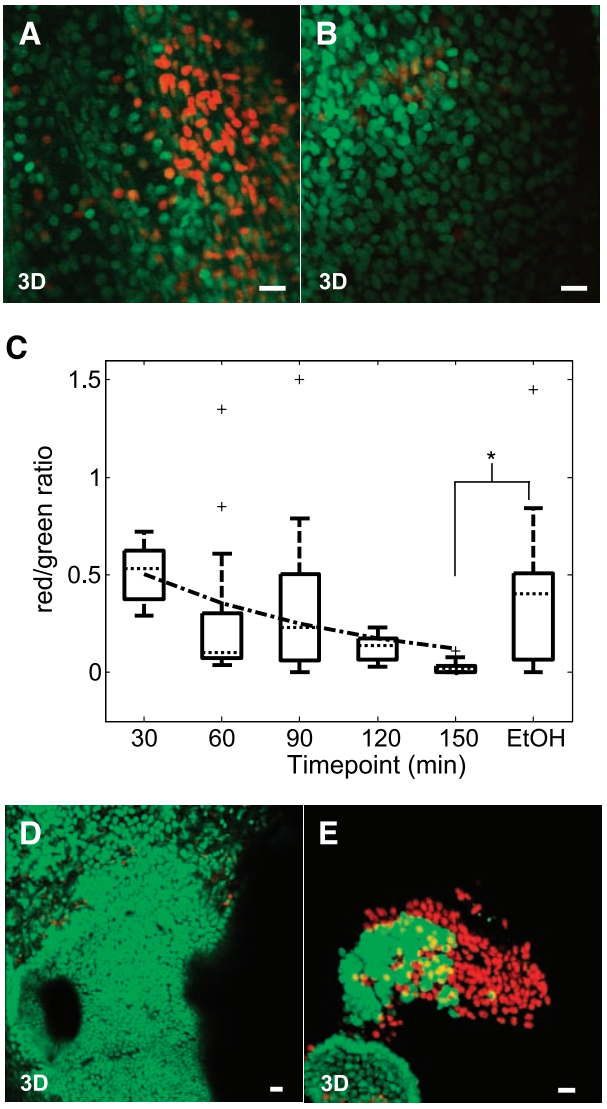

Figure 2. Assessment of incubation/imaging system with rapid viability assay. **A.** After 30 min in the incubation system, a three-dimensional projection of stained murine ovarian cells reveals a number of compromised (*red*) along with a majority of viable cells (*green*). **B.** A three-dimensional projection at 150 min of culture suggests the murine ovarian tissue was stabilized in the incubation system with minimal compromised cells (*red*) present among viable cells (*green*). **C.** Tissue responded to the incubation system in an adaptive manner. Using the ratio of red to green cells, initially, the murine tissue exhibited a number of compromised cells, but the amount decreased exponentially (*dashed line*) as the tissue remained in the incubation system with minimal compromised cells by 150 min. A subsequent insult to the tissue at 150 min with ethanol resulted in measurable cellular damage. *, $P = 0.003$, ANOVA linear contrast. +, outliers on the box-and-whisker diagram; *bars,* total extent of the data. **D.** A typical human ovary biopsy maintained in the incubation system remained viable following multiphoton imaging. **E.** In a case where the biopsy was not immediately placed in the incubation system, increased areas of compromised cells (*red*) were apparent. Bars, 20 μm.

a single layer above the collagen-dominated stroma correlating well with an H&E-stained section from the same general region (Fig. 3B). Originally, the 2PEF from the surface epithelium was convoluted with bright fluorescent structures (Fig. 3C), but removal of the punctate fluorescence (see Materials and Methods) produced an improved image of the intracellular 2PEF (Fig. 3D).

To confirm that intracellular 2PEF was related to NAD(P)H fluorescence, we introduced 8 mmol/L NaCN, a mitochondrial transport blocker that increases the pool of fluorescent NAD(P)H compared with non-fluorescent NAD^+ (30), to the culture media. An immediate increase in cytoplasmic fluorescence was evident (Fig. 3E and F) with intracellular fluorescence intensity increasing from 82.3 ± 8.29 arbitrary units (a.u.) pre-NaCN to 129.7 ± 9.3 a.u. 5 min post-NaCN. This increase in fluorescence signal both confirmed that a substantial contributor to the 2PEF signal originated from NAD(P)H-related fluorescence, and that the tissue was viable at the time of imaging reflected by the NaCN disruption of active mitochondria.

We next evaluated the key morphologic features based on 2PEF and SHG. Depending on the orientation of the tissue surface in relation to the incident light, 2PEF combined with SHG in normal biopsies revealed surface epithelium similar to en face imaging (Figs. 3A and 4A), a valuable configuration for assessing epithelial organization, as well as epithelial/stromal interface architecture in a transverse imaging orientation (Fig. 4C). In biopsies from patients diagnosed with ovarian cancer, abnormal morphologic changes were observed consistent with focal cellular proliferation (Fig. 4E), cells heterogeneous in shape and size (Fig. 4I and J), and change in collagen structure and integrity with depth (Fig. 4J and K). Interestingly, in nondiseased tissue described histologically as having focal epithelial stratification, perhaps an indicator of pre-neoplastic changes, we also observed abnormal areas of surface epithelial growth combined with altered collagen integrity (Fig. 4G).

We further investigated the importance of collagen fibrillar structure proximal to the epithelial surface with SHG. First, examining the normal samples, we found that the collagen of younger patients was more linearly structured with long, straight fibrils, whereas the collagen of older patients became more diffuse and curved in nature (Fig. 5A and B). To quantitatively assess these collagen-related changes, we applied GLCM texture analysis to the SHG images. The correlation feature extracted from the GLCM provided an estimate of collagen fibril organization and structure (29). Because this feature is an average from the entire image, images dominated by more defined, structured fibrils result in a substantial reduction in correlation with distance (steeper slope).

Consistent with qualitative appearances, we found that the correlation remained higher in older individuals (diffuse curved fibrils) with the $Corr_{50}$, the pixel distance where the correlation dropped below 50% of the initial value, significantly greater in patients older than 60 years compared with patients under 60 (Fig. 5C; $P = 0.02$, ANOVA linear contrast; $n_{30\text{-}49} = 7$; $n_{50\text{-}60} = 4$; $n_{>60} = 10$). Furthermore, we found a slight increase in the correlation between normal-low risk (LR) and normal-high risk (HR) samples in the group over 50 years (all

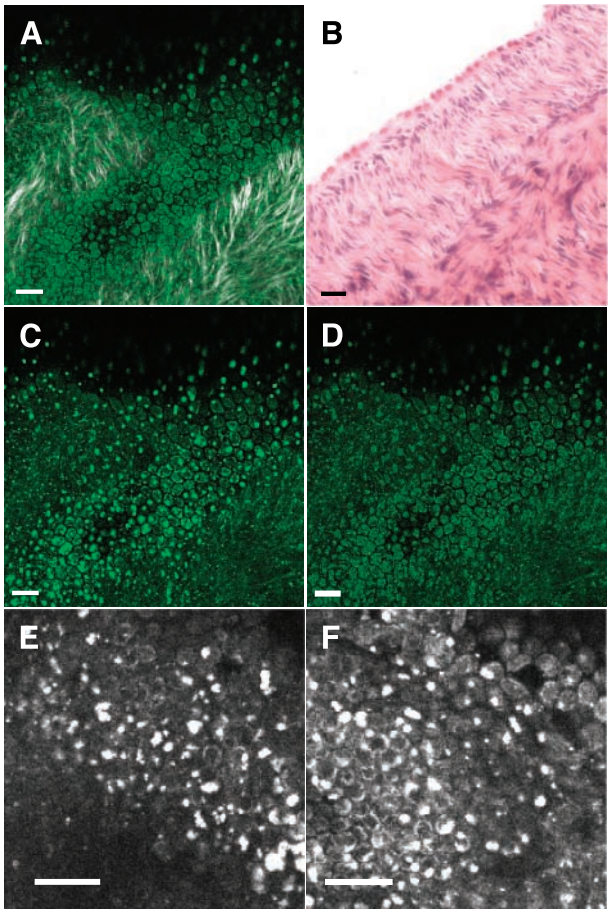

Figure 3. Endogenous contrast multiphoton images of ovarian biopsies. **A.** Multiphoton images consisted of intra- and extracellular 2PEF (*green*), as well as extracellular SHG (*grayscale*). The image of normal single-layer surface epithelium corresponds well with the (**B**) H&E-stained section from a nearby region. **C.** Bright punctate 2PEF was common and particularly associated with the surface epithelium. **D.** With image processing, the punctate fluorescence was removed to improve visualization of intracellular 2PEF. **E.** Pretreated 2PEF intensity increased dramatically (**F**) with the addition of NaCN verifying intracellular NAD(P)H-related 2PEF. Diffuse intracellular 2PEF increase was not accompanied by an increase in punctate fluorescence structures, and the two image planes pre- and post-NaCN are slightly offset because of tissue movement during manual introduction of NaCN to the imaging chamber. Bars, 20 μm.

postmenopausal), although the differences in this small sample were not significant (Fig. 5D; $n = 4$ for LR > 50; $n = 8$ for HR > 50).

In abnormal tissue, the collagen integrity was specifically compared between cancer samples and normal samples from the 50- to 60-year age group (all postmenopausal) because of similar ages of these two groups ($n = 4$ for normal; $n = 5$ for cancer). Visually, the SHG images in these two groups differed in structure with the normal biopsies exhibiting normotypic structured collagen fibrils near the epithelial surface (Fig. 5E) and the biopsies from patients with cancer exhibiting a loss of fine structure and structural organization with wavy, collagen bands (Fig. 5F). Interestingly, the biopsy from the 28-year-old patient with atypical surface epithelium (Fig. 4G) exhibited depleted collagen fibrils below this surface epithelial growth that seemed to have altered structural integrity (Fig. 5G).

Quantitatively, normal tissue correlation fell off sharply with distance, suggesting distinct, linear fibrils, whereas abnormal tissue correlation remained elevated as distance increased, suggestive of less defined fibrillar structure (Fig. 5H). The correlation in the cancer group was even greater with pixel distance than the correlation found in the older patient group (Fig. 5C). The collagen structure in cancer tissue appeared as wavy or crimped fibrils (Fig. 5F), whereas collagen fibrils in older patients appeared diffuse but still retained some normal fine structure (Fig. 5B). The $Corr_{50}$ of the normal group (age, 50-60) differed significantly from the $Corr_{50}$ of the cancer group (Fig. 5H, $P = 0.0006$, $n = 9$, two-tailed t test on log-transformed $Corr_{50}$). Moreover, the correlation of the SHG from the sample near the focal growth (Fig. 5G) was similar to the cancer group correlations (Fig. 5H, blue dashed line). As an alternative to the GLCM correlation feature analysis, we also evaluated spatial frequency characteristics of the SHG images. We observed that the lower spatial frequencies (≤10 μm^{-1}) increased, whereas the higher spatial frequencies (72-92 μm^{-1}) decreased in the cancer group compared with the normal group ($P < 0.0001$; $n = 37$; two-tailed t test on low versus high magnitude ratio), consistent with an alteration in collagen fibril fine structure (reduction of higher spatial frequencies) in the cancer group as observed with the correlation feature analysis.

Besides tissue morphologic and SHG-based texture features, we also implemented two-channel 2PEF to estimate cellular redox ratios, an estimate of aerobic metabolism, based on NAD(P)H- and FAD-related fluorescence. Using system calibration with NADH and FAD standards, we estimated the NAD(P)H and FAD contributions (Eqs. A and B) in the 2PEF images and used these to estimate the cellular redox ratio (Eq. C). The NAD(P)H-related signal dominated the intracellular fluorescence, although the FAD-related signal was measurable at low levels.

To calculate the redox ratio from intracellular 2PEF locations only, we segmented the images so that only cellular regions were analyzed (Fig. 6A and B). Using these segmented images, we calculated the redox ratio pixel by pixel to produce a redox distribution on the segmented images (Fig. 6C). In images where the cellular morphology distinctly differed within a field of view, we also assessed the redox ratio variation in morphologically different groups of cells. For example, in a normal-high risk sample, a population of large cells was located near a group of smaller, more compact cells (Fig. 6D). Comparing the redox ratio values in these two groups of cells, the values seemed similar (Fig. 6E); however, the smaller cells had a slightly lower and less variable redox ratio (0.11 ± 0.05) than the larger cells (0.12 ± 0.07). Besides this specific case, the redox ratio estimates typically exhibited little variance within a given field of view, so we compared the average redox values of epithelial regions between normal-low risk, normal-high risk, and abnormal ovaries from cancer samples. Normal-high risk

redox ratios were highly variable, falling between substantially separated normal-low risk and cancer redox ratios (Fig. 6F, $P = 0.053$, ANOVA linear contrast between low risk and cancer).

Discussion

We have developed an incubation/imaging system capable of transporting ovarian biopsies from the

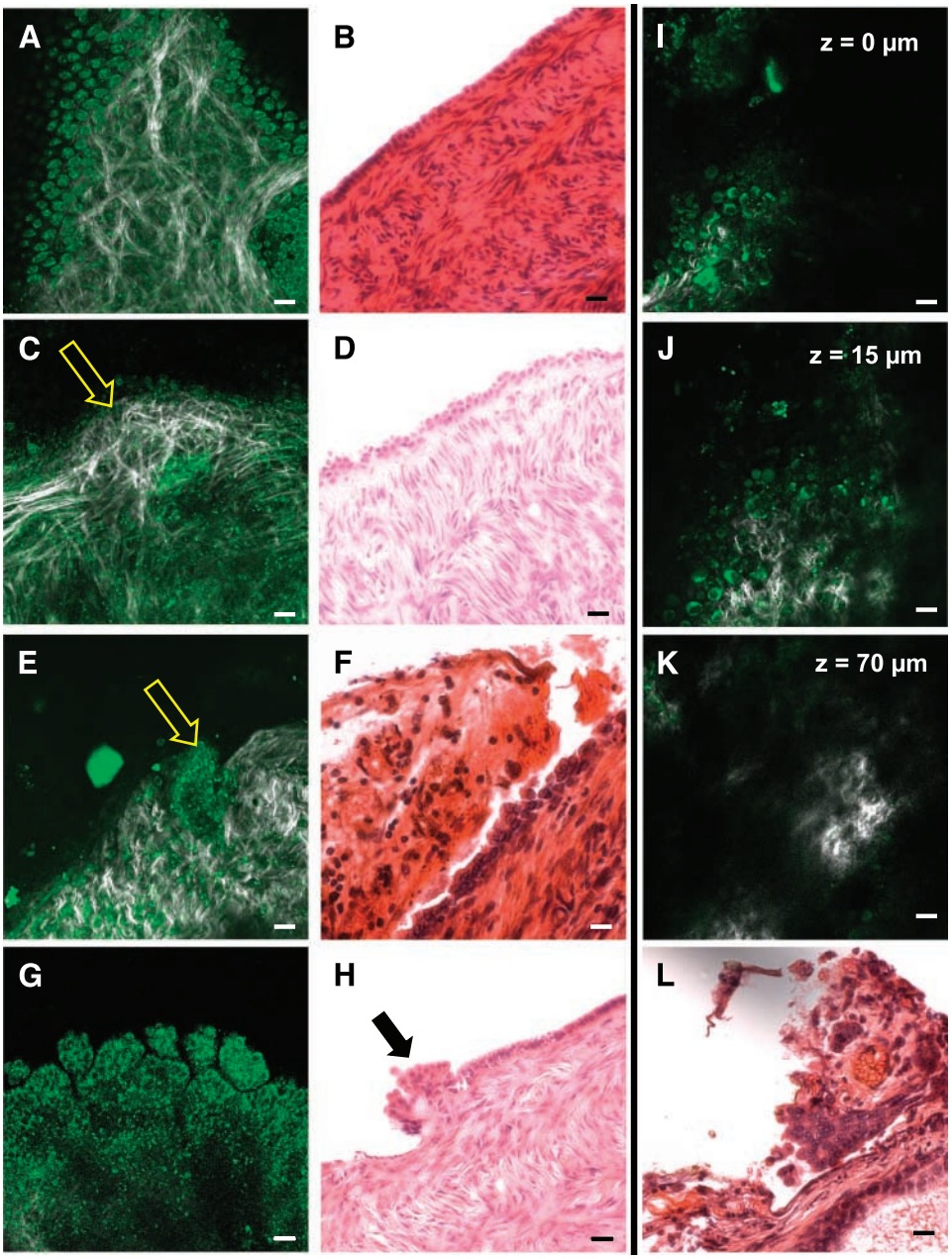

Figure 4. Morphologic features of normal and abnormal ovarian tissue. **A.** Large cells of a normal surface epithelium from a high-risk patient are well organized on top of highly structured collagen fibrils. Because of the convoluted geometry of the ovarian surface, these cells are on the side of a "hill," optically sliced to reveal the underlying collagen fibrils. **B.** Corresponding histology. **C.** Transverse imaging view of surface epithelium distinctly separated from collagen-dominated stroma (*arrow*). **D.** Corresponding histology. **E.** Abnormal tissue from a patient with cancer shows regions of concentrated cells (*arrow*) among mainly acellular regions of collagen fibrils. **F.** Corresponding histology. **G.** An abnormal region from a normal patient found to have epithelial stratification is consistent with cellular growth and altered collagen structure. **H.** Corresponding histology with similar cellular structures (*arrow*). An abnormal sample from a cancer sample shows cells of varying size at the surface (**I**) and subsurface (**J**), whereas with increased depth, the collagen is both depleted and lacks integrity (**K**). *z,* imaging depth. **L.** Corresponding histology. Bars, 20 μm.

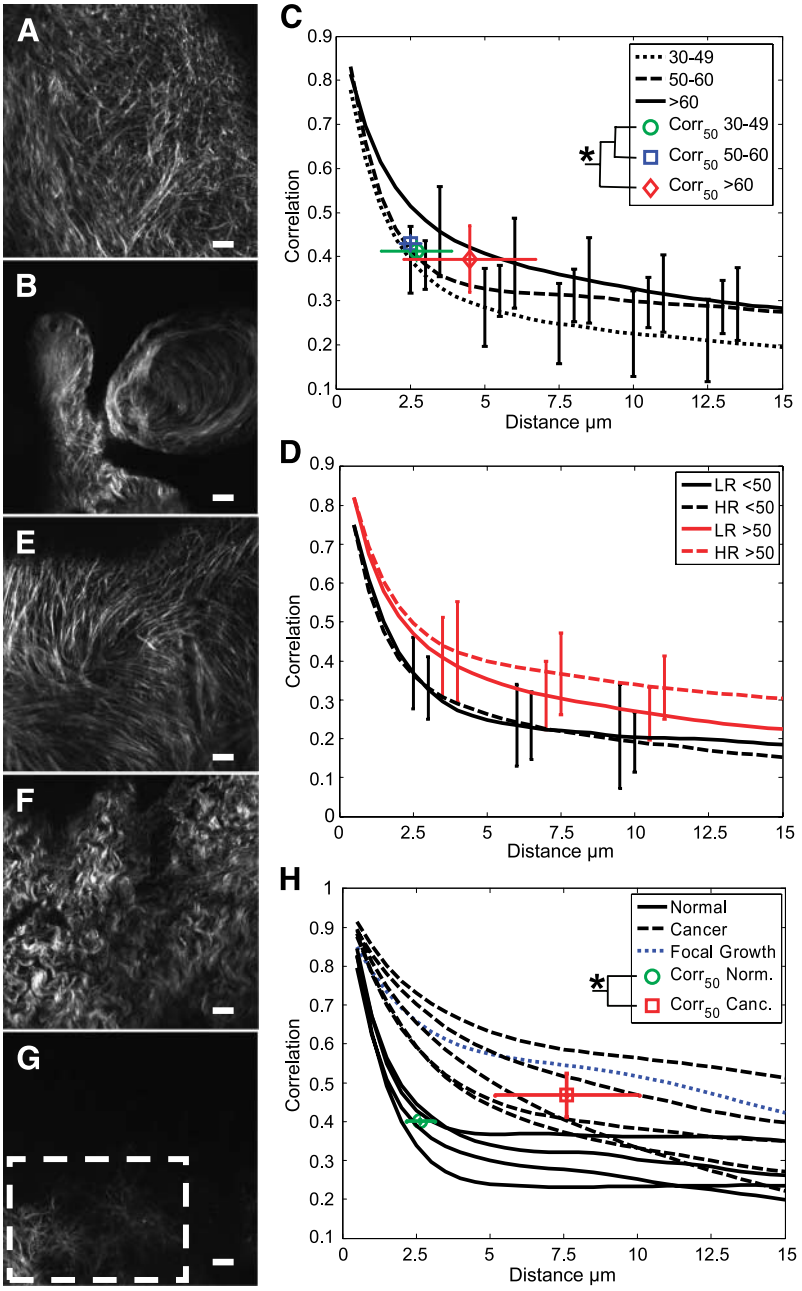

Figure 5. Analysis of collagen structure based on SHG. **A.** Collagen from a 42-year-old patient is highly structured with well-defined linear fibrils. **B.** In a sample from a 73-year-old patient, the collagen fibrils seem more diffuse and structurally curved. **C.** Quantitative age-related collagen changes showed that the correlation decreased less with distance in tissue from older patients (>60), consistent with the loss of linear fibril structure and definition as calculated with the $Corr_{50}$, the distance where the correlation crossed 50% of the initial correlation. *, $P = 0.02$, ANOVA linear contrast, $n_{30\text{-}49} = 7$; $n_{50\text{-}60} = 4$; $n_{>60} = 10$). **D.** Comparison between normal-low and normal-high risk samples showed increased correlation in the normal-high risk group from patients over 50 years [$n = 3$, low risk <50 years (LR < 50); $n = 4$, high risk <50 years (HR < 50); $n = 4$, low risk >50 years (LR > 50); $n = 8$, high risk >50 years (HR>50)]. **E.** In tissue from a patient 52 years old, the collagen fibrils are linear and highly structured. **F.** Collagen structure in an abnormal sample from a 50-year-old patient diagnosed with ovarian cancer reveals a marked change in collagen structure with crimped fibrils and thick bands. **G.** The collagen structure beneath focal growth in Fig. 4K from a 28-year-old patient also exhibits structural changes. Texture features were only calculated where collagen fibrils were observed (*white dashed box*). **H.** The cancer samples exhibited higher correlation with distance consistent with a loss of fine fibril structure. *, $P = 0.0006$; $n = 4$, normal; $n = 5$, cancer; two-tailed t test on log-transformed $Corr_{50}$ distance. The correlation from the focal growth was similar to the cancer group (*blue dashed line*). *Bars,* SD. Bars, 20 μm.

operating room to the microscope for multiphoton imaging in an environment that promotes consistent measurements of endogenous signals and extended experimental imaging periods. Our system allows tissue to be maintained in a stable environment over time, a critical element for measuring the functionally linked cellular endogenous signals and comparison with *in vivo* optical measurements.

Multiphoton images from the ovarian biopsies varied from diagnosis (normal versus cancer) as well as patient age and menopausal status. Several key features were observed in the images. First, when imaging normal surface epithelium, the cells were closely packed and were one to two layers thick with diffuse intracellular fluorescence accompanied by bright punctate fluorescence both inside and outside the cells. This homogenous size of cells and uniform distribution would be expected in normal ovarian surface epithelium similar to our observations using the confocal microendoscope (14). The epithelial surface of cancer tissue showed cells of varying sizes with multiple layers of these cells appearing to clump together, consistent with the histology of neoplastic tissue, including cellular proliferation and heterogeneity.

Another key feature extracted was the collagen structure and organization in the stroma based on the

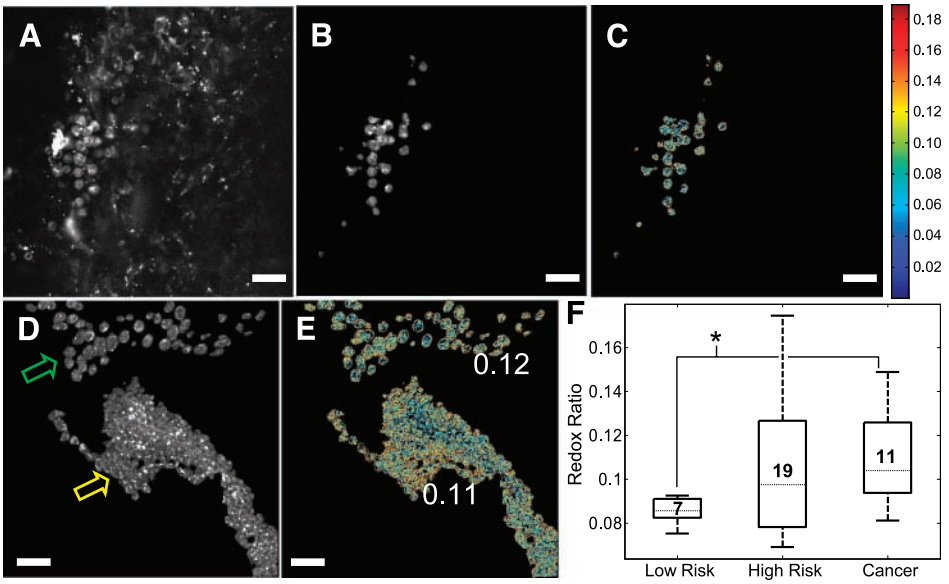

Figure 6. Application of two-channel intracellular 2PEF for estimation of cellular redox ratio. **A.** 2PEF image of both cellular and extracellular fluorescence. **B.** Based on FAD-related 2PEF estimation, cellular related 2PEF was segmented out. **C.** A redox ratio map of the segmented image calculated from NAD(P)H and FAD-related 2PEF reveals a distribution of intracellular redox ratio values. *Color bar,* redox ratio values for both **C** and **E**. **D.** In an image from a normal-high risk patient, a group of large (*green arrow*) and small cells (*yellow arrow*) are visible allowing for (**E**) localized redox ratio calculation for the two groups of cells. Values displayed are the mean redox ratio. **F.** An overall comparison of redox ratio values from tissue biopsies shows the greatest difference between normal-low risk and cancer groups. *, $P = 0.053$, ANOVA linear contrast. *Box-and-whisker numbers,* sample size for each group; *bars,* total extent of data. Bars, 20 μm.

SHG signal. Collagen structure in younger patients seemed different from older patients consistent with age-related collagen changes observed by others (31). Quantitatively, slight differences were found between normal-high risk and normal-low risk samples in the postmenopausal group, with the normal-high risk samples notably trending toward the cancer group. The collagen structure in the cancer seems similar to the wavy structure of collagen in a relaxed tendon and may reflect a loss of collagen cross-links or dysregulation of components maintaining normal collagen organization. Reduction in collagen SHG has been shown as a discriminating factor in oral malignancies (18); however, the changes to collagen SHG we observed related more to fibril structure than to loss of collagen. We also observed in one high-risk patient that collagen was structurally modified underneath focal areas of epithelial stratifications. The interaction between the extracellular matrix and transformed neoplastic cells is thought to be a key element of cancer-induced angiogenesis and invasion (32). Recent research suggests that basement membrane loss occurs in surface epithelium from high-risk ovaries (3), perhaps promoting abnormal cellular function and directly affecting remodeling of the underlying extracellular matrix. SHG may prove to be useful for the assessment of these lesions. Likewise, alternative technologies sensitive to collagen structure such as optical coherence tomography, scattering spectroscopy, and confocal reflectance microscopy may also show the ability to detect early ovarian cancer changes.

In addition to providing a morphologic representation of the surface epithelium, NAD(P)H in combination with FAD-related 2PEF allowed for an estimate of cellular metabolism. Somewhat surprisingly, the redox ratios from the surface epithelium of normal-low risk samples were the lowest, suggesting that this tissue had the highest aerobic mitochondrial metabolism, whereas normal-high risk samples had a highly variable redox ratio, and the cancer samples had the highest redox ratios. We hypothesize that the low, relatively consistent redox ratio of normal-low risk tissue reflects a normal functioning surface epithelium dependent on mitochondrial aerobic metabolism, whereas cells measured in abnormal tissue may have been substrate limited, therefore limiting their aerobic metabolism. In addition, invasive tumor cells often exhibit a glycolytic phenotype even in an aerobic environment (33). This phenotype may result in a higher redox ratio because the NAD(P)H pool might no longer be dominated by mitochondrial-related NAD(P)H. In normal-high risk patients, a large variability of redox values was observed consistent with the normal-high risk group spanning the spectrum between normal and cancer samples. Redox imaging with 2PEF sensitivity may be further improved by optimizing the detection of NAD(P)H and FAD-related 2PEF with multiwavelength excitation or fluorescence lifetime imaging, perhaps allowing for the identification of abnormal regions present in early ovarian neoplasms.

Taken together, these results suggest that, with our viable imaging system, we can qualitatively and quantitatively assess endogenous optical biomarkers of the

ovarian surface with multiphoton microscopy. Given the morphologic information present in multiphoton imaging of the ovary, this technique may potentially be translated to an *in vivo* corollary to histology as a so-called ''optical biopsy.'' Furthermore, the additional intriguing results from this study regarding the collagen structure beneath the surface epithelium and redox ratio of the surface epithelium may provide sensitive biomarkers in ovarian cancer as well as aid in the elucidation of early processes in ovarian carcinogenesis.

References

1. U.S. Cancer Statistics Working Group. United States cancer statistics: 2003 incidence and mortality. Atlanta: US Department of Health and Human Services, Centers for Disease Control and Prevention and National Cancer Institute; 2006.
2. Modugno F. Ovarian cancer and high-risk women—implications for prevention, screening, and early detection. Gynecol Oncol 2003;91: 15–31.
3. Roland IH, Yang WL, Yang DH, et al. Loss of surface and cyst epithelial basement membranes and preneoplastic morphologic changes in prophylactic oophorectomies. Cancer 2003;98:2607–23.
4. Bhoola S, Hoskins WJ. Diagnosis and management of epithelial ovarian cancer. Obstet Gynecol 2006;107:1399–410.
5. Bast RC, Jr., Berek JS, Obrist R, et al. Intraperitoneal immunotherapy of human ovarian carcinoma with *Corynebacterium parvum*. Cancer Res 1983;43:1395–401.
6. Luo LY, Katsaros D, Scorilas A, et al. The serum concentration of human kallikrein 10 represents a novel biomarker for ovarian cancer diagnosis and prognosis. Cancer Res 2003;63:807–11.
7. Mor G, Visintin I, Lai Y, et al. Serum protein markers for early detection of ovarian cancer. Proc Natl Acad Sci U S A 2005;102:7677–82.
8. Olivier RI, Lubsen-Brandsma MA, Verhoef S, van Beurden M. CA125 and transvaginal ultrasound monitoring in high-risk women cannot prevent the diagnosis of advanced ovarian cancer. Gynecol Oncol 2006;100:20–6.
9. Puls L, Powell D, DePriest P, et al. Transition from benign to malignant epithelium in mucinous and serous ovarian cystadenocarcinoma. Gynecol Oncol 1992;47:53–7.
10. Kurtz AB, Tsimikas JV, Tempany CM, et al. Diagnosis and staging of ovarian cancer: comparative values of Doppler and conventional US, CT, and MR imaging correlated with surgery and histopathologic analysis—report of the Radiology Diagnostic Oncology Group. Radiology 1999;212:19–27.
11. McWilliams A, MacAulay C, Gazdar AF, Lam S. Innovative molecular and imaging approaches for the detection of lung cancer and its precursor lesions. Oncogene 2002;21:6949–59.
12. Georgakoudi I, Jacobson BC, Muller MG, et al. NAD(P)H and collagen as *in vivo* quantitative fluorescent biomarkers of epithelial precancerous changes. Cancer Res 2002;62:682–7.
13. Benavides JM, Chang S, Park SY, et al. Multispectral digital colposcopy for *in vivo* detection of cervical cancer. Opt Express 2003;11:1223–36.
14. Brewer MA, Utzinger U, Barton JK, et al. Imaging of the ovary. Technol Cancer Res T 2004;3:617–27.
15. Zipfel WR, Williams RM, Webb WW. Nonlinear magic: multiphoton microscopy in the biosciences. Nat Biotechnol 2003;21: 1369–77.
16. Zoumi A, Yeh A, Tromberg BJ. Imaging cells and extracellular matrix *in vivo* by using second-harmonic generation and two-photon excited fluorescence. Proc Natl Acad Sci U S A 2002;99:11014–9.
17. Skala MC, Squirrell JM, Vrotsos KM, et al. Multiphoton microscopy of endogenous fluorescence differentiates normal, precancerous, and cancerous squamous epithelial tissues. Cancer Res 2005;65:1180–6.
18. Wilder-Smith P, Osann K, Hanna N, et al. *In vivo* multiphoton fluorescence imaging: a novel approach to oral malignancy. Lasers Surg Med 2004;35:96–103.
19. Campagnola PJ, Loew LM. Second-harmonic imaging microscopy for visualizing biomolecular arrays in cells, tissues and organisms. Nature Biotechnol 2003;21:1356–60.
20. Wang KH, Majewska A, Schummers J, et al. *In vivo* two-photon imaging reveals a role of arc in enhancing orientation specificity in visual cortex. Cell 2006;126:389–402.
21. Campagnola PJ, Wei MD, Lewis A, Loew LM. High-resolution nonlinear optical imaging of live cells by second harmonic generation. Biophys J 1999;77:3341–9.
22. Kirkpatrick ND, Zou CP, Brewer MA, Brands WR, Drezek RA, Utzinger U. Endogenous fluorescence spectroscopy of cell suspensions for chemopreventive drug monitoring. Photochem Photobiol 2005;81:125–34.
23. Huang S, Heikal AA, Webb WW. Two-photon fluorescence spectroscopy and microscopy of NAD(P)H and flavoprotein. Biophys J 2002; 82:2811–25.
24. Zipfel WR, Williams RM, Christie R, Nikitin AY, Hyman BT, Webb WW. Live tissue intrinsic emission microscopy using multiphoton-excited native fluorescence and second harmonic generation. Proc Natl Acad Sci U S A 2003;100:7075–80.
25. Williams RM, Zipfel WR, Webb WW. Interpreting second-harmonic generation images of collagen I fibrils. Biophys J 2005;88:1377–86.
26. Palmer GM, Marshek CL, Vrotsos KM, Ramanujam N. Optimal methods for fluorescence and diffuse reflectance measurements of tissue biopsy samples. Lasers Surg Med 2002;30:191–200.
27. Patterson GH, Knobel SM, Arkhammar P, Thastrup O, Piston DW. Separation of the glucose-stimulated cytoplasmic and mitochondrial NAD(P)H responses in pancreatic islet β cells. Proc Natl Acad Sci U S A 2000;97:5203–7.
28. Kloppenburg P, Zipfel WR, Webb WW, Harris-Warrick RM. Highly localized Ca(2+) accumulation revealed by multiphoton microscopy in an identified motoneuron and its modulation by dopamine. J Neurosci 2000;20:2523–33.
29. Kirkpatrick ND, Hoying JB, Botting SK, Weiss JA, Utzinger U. *In vitro* model for endogenous optical signatures of collagen. J Biomed Opt 2006;11:054021.
30. Eng J, Lynch RM, Balaban RS. Nicotinamide adenine dinucleotide fluorescence spectroscopy and imaging of isolated cardiac myocytes. Biophys J 1989;55:621–30.
31. Lin SJ, Wu R, Jr., Tan HY, et al. Evaluating cutaneous photoaging by use of multiphoton fluorescence and second-harmonic generation microscopy. Opt Lett 2005;30:2275–7.
32. Kurban G, Hudon V, Duplan E, Ohh M, Pause A. Characterization of a von Hippel Lindau pathway involved in extracellular matrix remodeling, cell invasion, and angiogenesis. Cancer Res 2006;66: 1313–9.
33. Gatenby RA, Gillies RJ. Why do cancers have high aerobic glycolysis? Nat Rev Cancer 2004;4:891–9.

Endogenous Optical Biomarkers of Ovarian Cancer Evaluated with Multiphoton Microscopy

Nathaniel D. Kirkpatrick, Molly A. Brewer and Urs Utzinger

Cancer Epidemiol Biomarkers Prev 2007;16:2048-2057.